Green Preparation of Nanoporous Pyrrhotite by Thermal Treatment of Pyrite as an Effective Hg(II) Adsorbent: Performance and Mechanism

Ping Lu, Tianhu Chen *, Haibo Liu, Ping Li, Shuchuan Peng and Yan Yang

Laboratory for Nano-minerals and Environmental Materials, School of Resources and Environmental Engineering, Hefei University of Technology, Hefei 230009, China; luping9305@163.com (P.L.); liuhaibosky116@hfut.edu.cn (H.L.); liping@hfut.edu.cn (P.L.); Pengshuchuan@hfut.edu.cn (S.P.); yan.yang@ucd.ie (Y.Y.)
* Correspondence: chentianhu@hfut.edu.cn; Tel.: +86-0551-62903990

check for updates

Abstract: The removal of Hg(II) from aqueous solutions by pyrrhotite derived from the thermal activation of natural pyrite was explored by batch experiments. The adsorption isotherms demonstrated that the sorption of Hg(II) by modified pyrite (MPy) can be fitted well by the Langmuir model. The removal capacity of Hg(II) on MPy derived from the Langmuir model was determined to 166.67 mg/g. The adsorption process of Hg(II) on MPy was well fitted by a pseudo-second-order model. The sorption of Hg(II) on MPy was a spontaneous and endothermic process. The removal of Hg(II) by MPy was mainly attributed to a chemical reaction resulting in cinnabar formation and the electrostatic attraction between the negative charges in MPy and positive charges of Hg(II). The results of our work suggest that the thermal activation of natural pyrite is greatly important for the effective utilization of ore resources for the removal of Hg(II).

Keywords: pyrite; thermal treatment; pyrrhotite; Hg(II) removal; mechanism

1. Introduction

With the rapidly increasing industrialization, heavy metal pollution has received increasingly more attention by the populace. Heavy metal ions are highly toxic even at low concentrations, and when released into the environment, they can cause devastating public health hazards [1,2]. As one of the most toxic metals ever discovered, Hg(II) is carcinogenic and stable with high cellular toxicity. Research has shown that Hg(II) can cause considerable damage to human health by causing toxicity to the central nervous system, kidneys, lung tissues, and reproductive system, resulting in health problems including paralysis, dysfunction of the central nervous system, intestinal and urinary complications, and even death in extreme cases [3,4]. Furthermore, trace amounts of Hg(II) in water are puzzling due to its complexation and mobility features at low concentrations, bioaccumulation during metabolic processes, wide distribution, and control difficulties. The United States Environment Protection Agency set a mandatory discharge limit of 10 μg/L for the total mercury content in wastewater, and the limit in drinking water is 1 μg/L [5]. Hence, it is very important to remove Hg(II) effectively from wastewater [6,7].

Various techniques have been put forward for aqueous Hg(II) removal such as electrolysis, precipitation, coagulation co-precipitation, membrane filtration, ionic exchange, and adsorption methods [8]. Among them, adsorption methods have been widely studied because they are cost-effective, environmentally friendly, and easy to conduct. Numerous adsorbents have been extensively studied, such as activated carbon [9,10], lichens [11], amine-modified attapulgite [8], poly(2-aminothiazole) [12], and mesoporous silica [5]. However, those adsorbents are either too costly

or have low adsorption capacity. Recently, many researchers have committed to the application of natural mineral materials as adsorbents due to their low cost and physicochemical properties. Hg(II) sorption to sulfides is a potentially important Hg(II) sequestration mechanism due to the strong chemical bond between Hg(II) and sulfur [13].

The application of natural pyrite is limited by the low adsorption capacity because of its low specific surface area and the strong S–S bond in the crystal structure. Natural pyrrhotite ($Fe_{1-x}S$, $0 < X < 0.125$) as a reactive iron sulfide mineral has a nanostructure but a small specific surface area [14]. Therefore, in order to gain highly reactive products, our group developed a cost-effective method by thermally activating pyrite [15]. Thermally activated pyrrhotite as a promising adsorbent has been studied for the removal of various contaminants, such as Cu(II) [16], Pb(II) [17,18], U(VI) [19], and Hg^0 [20]. They all exhibit excellent adsorption characteristics. Therefore, it is valuable to explore the remove of Hg(II) from wastewater using modified pyrite (MPy) in detail [21]. The widespread application of the modified pyrite as a filtering media or a recyclable magnetic sorbent for the remediation of Hg(II)-polluted environments is of great importance.

In this work, batch experiments are conducted to study the feasibility of MPy as a medium for adsorbing Hg(II). The objectives of this work are to fabricate nanoporous and magnetically recycled MPy to explore the properties and mechanisms of Hg(II) removal with MPy and to explore the application of pyrite as an effective adsorbent in environmental cleanup. It is believed that the experimental data are helpful for the application of MPy for Hg(II) removal.

2. Experimental Procedure

2.1. Sample Preparation

MPys were prepared by calcinating the natural pyrite in an N_2 atmosphere at different temperatures (550, 600, 700, 800 °C) for 0.5 h. Natural pyrite was collected from the Lujiang Mine, Anhui Province, China. First, the pyrite was fractured and ground to 74 μm. Then, the sample was soaked for 2 h with 5% HCl to remove the oxidation film and washed by Milli-Q water 4 times. The obtained samples were dried using a lyophilizer and then kept in a drier. Thermally-activated samples at different temperatures were obtained by setting different heating times. The as-prepared samples were labeled MPy-*T* (*T* denotes the annealing temperature). For instance, MPy-550 means that the pyrite was thermally treated at 550 °C.

2.2. Characterization

The phase composition of MPy was observed using XRD (Dandonghaoyuan 2700, D/max-rB, Rigaku, Tokyo, Japan, a voltage of 40 kV, an electric current of 30 mA, and ascan rate of 4°/min). The morphology and size distribution of MPy were characterized through gold-sputtering, field emission scanning electron microscopy (SEM, SU8020, Hitachi, Tokyo, Japan), and transmission electron microscopy (TEM, JEM-2100F, JEOL, Tokyo, Japan). The zeta potentials of MPy were recorded by a Zetasizer Nano ZS (Nano-ZS90, Malvern Panalytical Ltd, Malvern, UK). Thermogravimetric analysis and differential thermal analysis (TG-DTA) were performed on a Thermogravimetric Analyzer (TG/DTA7300, NSK, Tokyo, Japan). The hysteresis loop of MPy was demonstrated using MPMS (MPMS XL-7, Quantum Design, Inc., San Diego, CA, USA). X-ray photoelectron spectra (XPS) of Fe2p, S2p, O1s, and Hg4f spectral regions were characterized using X-ray photoelectron spectroscopy (Thermo, ESCALAB 250Xi, Thermo Fisher Scientific, Waltham, MA, USA). IR spectra of MPy were examined using a Fourier transform infrared spectrometer (FTIR, Vertex-70, KBr, Bruker, Ettlingen, Germany). The spectra were recorded using a Raman spectrometer (Horiba Jobin Yvon, HR Evolution, HORIBA Scientific, Kyoto, Japan) with a laser at 532 nm in these experiments.

2.3. Batch Experiments

In this research, batch experiments were conducted to evaluate the performance of MPy on Hg(II) adsorption. The solution of Hg(II) was obtained by dissolving $HgNO_3$ (analytically pure) in pure water, and the pH was adjusted to 3 for preservation. The effect of the activation temperature was evaluated by 1.0 g/L MPy prepared at different temperatures in different Hg(II)concentrations in the presence of 0.01 mol/L $NaNO_3$ for 24 h. The performance of suspension pH and ionic strengths was explored with 1.0 g/L MPy-600 at the range of 2.0–7.0 by using trace amounts of 0.01–1.0 mol/L HNO_3 and NaOH solution in 10 mg/L of Hg(II) for 210 min. The effect of the adsorbent dose on Hg(II) adsorption was evaluated by adding a different concentration (0.2–1.0 g/L) of MPy-600 in 20 mg/L of Hg(II) in the presence of 0.01 mol/L $NaNO_3$ at pH 6 for 24 h. The kinetic analysis was explored with 0.4 g/L MPy-600 in 10 mg/L of Hg(II) in the presence of 0.01 mol/L $NaNO_3$. The effect of the reaction temperature was investigated at different temperatures (298, 308 and 318 K). After the reaction, the solid-liquid phases were separated with the 0.22 μm membrane. The content of residual Hg(II) in the solution was measured using a direct mercury analyzer (DMA-80, Milestone Systems, Borneo Municipality, Denmark). The removal (adsorption, %) and sorption capacity (Qs, mg/g) were obtained by Equations (1) and (2), respectively:

$$Adsorption(\%) = (C_0 - C_e)/C_0 \times 100\% \tag{1}$$

$$Q_s = V \times (C_0 - C_e)/m \tag{2}$$

where C_0 (mg/L) is the starting concentration, C_e (mg/L) is the concentration after adsorption, V (L) is the suspension volume, and m (g) is the mass of adsorbent.

3. Results and Discussion

3.1. Characterization of Naturally Derived Pyrrhotite

Figure 1A shows the XRD spectrum of natural pyrite and MPy calcined at different temperatures. The appearance of a weak peak of MPy-550 at 2θ = 44.08° indicates the formation of monoclinic pyrrhotite. When the calcination temperature is 600 °C, the disappearance of the reflections of pyrite demonstrates that pyrite is completely decomposed into monocline pyrrhotite. The enhancement in the reflections of MPy-700 suggests a higher crystallinity. As the temperature rises to 800 °C, monoclinic pyrrhotite translates into hexagonal pyrrhotite [22].
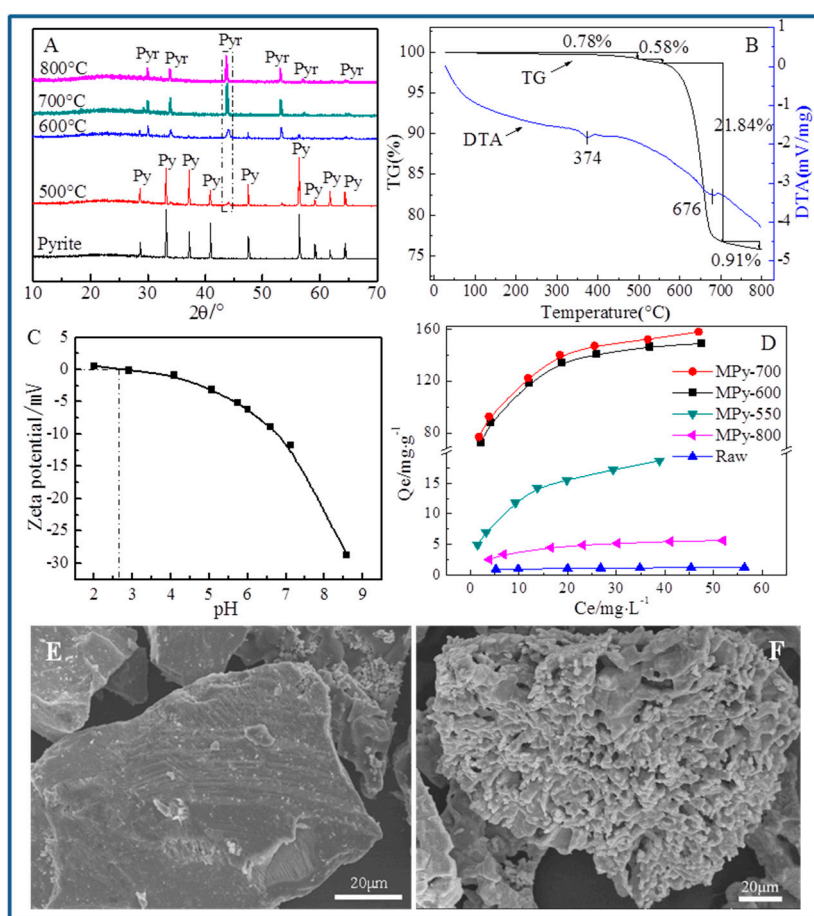
Figure 1. (**A**) XRD spectrum of natural pyrite and MPy. Py—pyrite; Pyr—pyrrhotite. (**B**) TG-DTA spectrum of natural pyrite in a N_2 atmosphere. (**C**) The zeta potential of MPy-600. (**D**) Removal isotherms of Hg(II) by pyrite and MPy. (**E,F**) SEM images of natural pyrite and MPy-600, respectively.

Apparently, from the TG curve in Figure 1B, four weight loss stages are found in the thermal degradation of pyrite. However, the DTA curves reveal two endothermic peaks that correspond well to the weight losses. The first region (under 493 °C) and the endothermic peak at 374 °C due to the dehydration and dehydroxylation. The second region (493–531 °C) is associated with the process of ferrous sulfate decomposed to hematite and sulfur dioxide gas [23]. The third region (531–697 °C) and the endothermic peak at 676 °C corresponds to the process that the pyrite transformed to pyrrhotite by desulfuring as follows in Equation (3) [18]. Lastly, the fourth region (under 800 °C) is assigned to the conversion of monoclinic pyrrhotite to hexagonal pyrrhotite [24].

$$FeS_2 \rightarrow Fe_{1-X}S + S \tag{3}$$
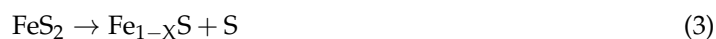
The zeta potential of MPy-600 is shown in Figure 1C. The pH_{ZPC} (zero-point charge) of MPy-600 is observed at pH 2.6. The findings indicate that the negative charge of the MPy-600 surface is obtained by releasing protons at pH > 2.6. The MPy-600 surface possesses positive charges by protonating amphoteric ions at pH < 2.6 [25]. SEM images of natural pyrite and MPy-600 are shown in Figure 1E,F. The crystal size of natural pyrite is large with no porous texture. However, the MPy-600 surface has nanometer-sized structures with abundant inhomogeneous pores that provide ample active sites and high activity.

3.2. Adsorption Isotherms

The sorption capacities of Hg(II) on pyrite and MPy calcined at different temperatures are presented in Figure 1D. The removal of Hg(II) by MPy and pyrite obviously increases with the initial concentration increase. The sorption capacities of MPy-600 and MPy-700 are higher than those of the other samples because of the nanoporous structure and high specific surface area (27.62 m^2/g) [15]. According to the research results, MPy-600 is an ideal material for the study of Hg(II) removal with respect to the consumed energy for grinding. The saturated sorption capacity is approximately 148.65 mg/g. The sorption process of Hg(II) by MPy-600 can be matched by the Langmuir model and the Freundlich model. The Langmuir type describes monolayer sorption which has identical and equal-energy sorption sites, while the Freundlich type is used for heterogeneous adsorption.

Langmuir isotherm:

$$\frac{C_e}{Q_e} = \frac{1}{Q_m K_L} + \frac{C_e}{Q_m} \tag{4}$$

Freundlich isotherm:

$$lnQ_e = lnK_F + \frac{1}{n}lnC_e \tag{5}$$

where C_e is the equilibrium concentration (mg/L), Q_e is the equilibrium sorption capacity (mg/g), Q_m is the saturated sorption capacity (mg/g), K_L is the Langmuir sorption constant (L/mg), K_F is the equilibrium coefficient ((mg/g)/(mg L)$^{-n}$), and $1/n$ is the sorption exponent associated with the heterogeneity of sorption sites. The D-R (Dubinin-Radushkevich) isotherm is more applicable than the Langmuir, and it assumes neither a uniform sorption potential nor a homogeneous surface. The D-R model in a linear formation can be expressed as:

$$q_e = q_m exp\left(-\beta\varepsilon^2\right) \tag{6}$$

where β is the activity coefficient of the average sorption energy (mol^2/kJ^2) and ε is the Polanyi potential, which is equivalent to:

$$\varepsilon = RTln\left(1 + \frac{1}{C_e}\right) \tag{7}$$

where R (8.314 J/(mol·K)) is an ideal gas constant, and T (K) is the absolute temperature in Kelvin (K). E (kJ/mol) represents the free energy change. The value of E can be calculated using the following expression:

$$E = \frac{1}{\sqrt{2\beta}} \tag{8}$$

The magnitude of E can provide an idea regarding the type of adsorption process, that is, whether the process is physical or chemical. When E is below 8 kJ/mol, the adsorbent process is considered to be physical. When E ranges from 8 to 16 kJ/mol, the adsorbent process is triggered by ion exchange. If the value of $E > 16$ kJ/mol, then the adsorbent process is of chemical properties.

The relative parameters of the above models are presented in Table 1. It can be inferred that the Langmuir type ($R^2 = 0.9991$) fit the experimental data better regarding the sorption of Hg(II) onto MPy-600 compared with Freundlich model ($R^2 = 0.9724$). This fact indicates that the adsorption of Hg(II) onto MPy-600 is monolayer sorption. The Q_m calculated from the Langmuir model is 166.67 mg/g. The maximum sorption capacity q_m worked out from the D-R model is lower than the Langmuir model, which may be ascribed to the different hypotheses of the sorption models [26,27]. A contrast of the Q_m in Table 2 indicates that MPy-600 presents a high adsorption ability of Hg(II).

Table 1. Isotherm parameters of the Langmuir, Freundlich, and D-R models.

Models	Parameters			
Langmuir	Q_m (mg/g)		K_L (L/mg)	R^2
	166.67		0.30	0.9991
Freundlich	k_F ((mg/g)/(mg L)$^{-n}$)		$1/n$	R^2
	63.06		0.22	0.9724
D-R	β (mol^2/kJ^2)	q_m (mg/g)	E (kJ/mol)	R^2
	6.06×10^{-6}	149.66	287	0.9879

Table 2. Comparison of the maximum adsorption capacities (Q_{max}) of Hg(II) on various adsorbents.

Material	Experimental Conditions	Q_{max} (mg/g)	References
Lichens	pH 6.0, 293 K	82.5	[11]
Activated carbon made from sago waste	pH 5.0, 303 K	55.6	[9]
MPy-600	pH 6.0, 303 K	166.7	this work
Activated carbon derived from (AEC)	pH 5.0, 303 K	28.4	[10]
Amine-modified attapulgite	pH 6.0, 298 K	93.2	[8]
Synthesis of poly (2-aminothiazole)	pH 6.5, 288 K	291.5	[12]
Al2O3-supported nanoscale FeS	pH 6.0, 303 K	142.7	[28]

3.3. The Effects of pH and Ionic Strength

The impact of pH and ionic strength on the Hg(II) sorption by MPy-600 is presented in Figure 2. The pH of the solution plays a large role in the removal of Hg(II) onto MPy-600. The removal quantity of Hg(II) rises from 0.8 to 4.3 mg/g as the pH varies from 2–6. However, with a further increase of pH from 6.0–7.0, the adsorption capacity exhibited a negligible change. According to the pH$_{PZC}$ of MPy-600, when pH < 2.6, the surface charge is positive. However, for pH > 2.6, the MPy-600 surface presents an abundant negative surface charge. Figure 2Bshows the Hg(II) species distribution in the solution. Hg(II) mainly exists as Hg^{2+} species at a pH < 3.1. But at the pH of 3–3.5, 40% of Hg(II) exists as Hg^{2+} species, 40% of Hg(II) exists in the form of Hg(OH)$_2$, and 20% of Hg(II) exists in the form of Hg(OH)$^+$.Furthermore, 50% of Hg(II) exists in the form of Hg(OH)$_2$, and 50% of Hg(II) exists in the hydrolyzed mononuclear and multinuclear species (i.e., Hg^{2+}, Hg$_2$(OH)$^{3+}$, Hg$_3$(OH)$_3^{3+}$, and Hg(OH)$^+$) at a pH range of 3.5–4.0. Hg(OH)$_2$ is the main variety of the Hg(II) aqueous solution at a pH > 4.0. Consequently, the slightly increased adsorption of Hg(II) onto MPy-600 at pH < 3 probably ascribes to the electrostatic repulsion between Hg^{2+} and the positive surface, and also the competition adsorption between the Hg(II) and H$^+$ of the binding sites on the MPy-600. The increased adsorption at the pH range from 3.0–6.0 can be ascribed to the electrostatic attraction which occurs between the positive charges of Hg(II) (i.e., Hg$_2$(OH)$^{3+}$, Hg$_3$(OH)$_3^{3+}$, Hg(OH)$^+$) and the negative MPy-600 surface. When the pH > 6.0, the adsorption capacity exhibits a neglectable change that is caused by the formation or precipitation of the hydroxyl complexes by metal ions. Given all these considerations, an initial pH of 6.0 is suitable as the optimal value for Hg(II) adsorption [3,11].

The impact of the ionic strength on the adsorption of Hg(II) onto MPy-600 is observed in Figure 2A. As presented in Figure 2A, with the increase of ion strength, the sorption of Hg(II) by MPy-600 increases. The electrical conductivity of the solution increases, which strengthens the electrostatic attraction of Hg(II) to the surface of MPy-600. It is certified that the inner surface complexation is irrelevant to the ionic strength, otherwise, the outer surface complexation is more sensitive to it. Consequently, this infers that the outer surface complexation mainly dominated the sorption process of Hg(II) onto MPy-600 [1,29]. It can be speculated that Hg(II) adsorbed on the MPy-600is due to the newly formed ferric hydroxide.
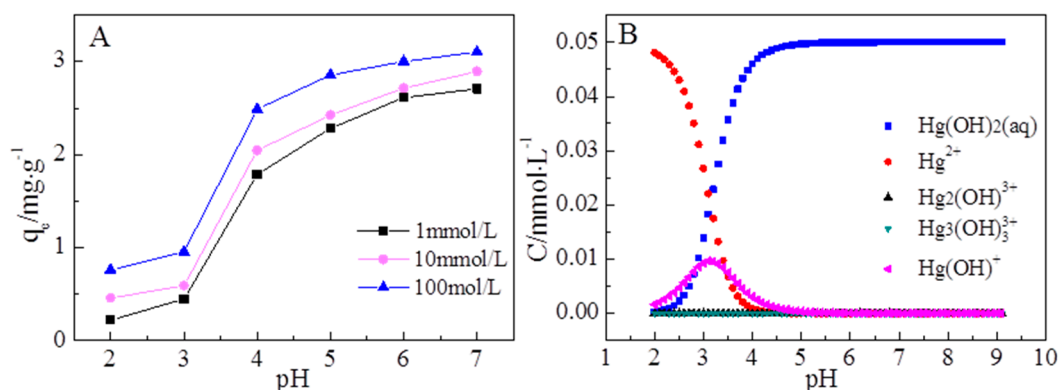
Figure 2. (**A**) The effect of pH and ionic strength. (**B**) Distribution of Hg(II) in water solutions (C_0 = 10 mg/L, I = 0.01 mol/L, T = 303 K).

3.4. The Effect of the AdsorbentDose

The impact of the MPy-600 concentration (0.2–1.0 g/L) on Hg(II) adsorption is presented in Figure 3. As presented in Figure 3, the removal rate of Hg(II) by MPy-600 increases with increasing adsorbent dose, whereas the removal quantity correspondingly decreases. With the increase of the adsorbent dose, there are more active sites available for sorption of Hg(II), which is more likely to facilitate penetration of Hg(II) to the adsorption points. The removal is turned up to be 80% at an MPy-600 concentration of 0.4 g/L. A further increase in MPy-600 concentration over 0.4 g/L does not lead to an obvious improvement in the removal but a reduction in the removal quantity of Hg(II) because of the surplus adsorption sites related to the quantity of the Hg(II) solution. Hence, the optimalMPy-600 concentration is 0.4 g/L for further experiments.
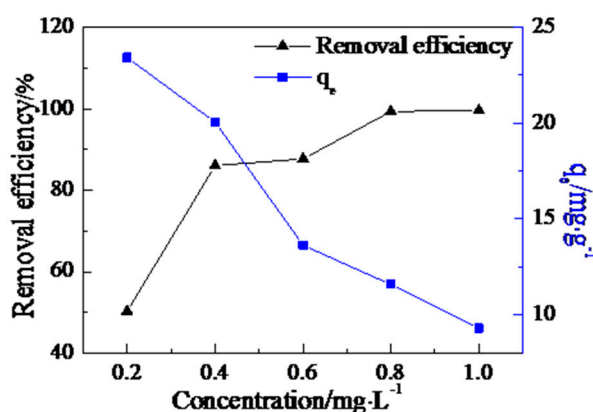

Figure 3. The effect of MPy-600 concentration on the adsorption of Hg(II).

3.5. Adsorption Kinetics

Adsorption kinetics measurements are conducted to estimate the performance of Hg(II) on MPy-600andto develop an understanding of the underlying mechanisms of Hg(II) adsorption on this sorbent and the potential rate-controlling steps through valuable data. As given in Figure 4A, the sorption capacity of Hg(II) onto MPy-600 distinctly increases with the increasing reaction time from 0–240 min, and the adsorption capacity rises slowly until equilibrium is attained during the experimental time period. To gain more information about the mechanisms, the data of the adsorption process are fitted with three model equations: The pseudo-first-order model, pseudo-second-order model, and Weber-Morris intraparticle diffusion model.

The pseudo-first-order and pseudo-second-order models are rate controlled, which is the strength of the adsorption capacity other than the solution concentration. Their linear forms of those models are given in Equations (9) and (10):

$$ln(q_e - q_t) = lnq_e - \frac{k_1}{2.303}t \tag{9}$$

$$\frac{t}{q_t} = \frac{1}{k_2 q_e^2} + \frac{t}{q_e} \tag{10}$$

where q_e (mg/g) and q_t (mg/g) represent the quantity of metal adsorbed at equilibrium and at a certain time, respectively, t (min) represents time, k_1 is the adsorption rate constants (g/(mg·min)) of the pseudo-first-order kinetic model, and k_2 is the adsorption rate constants (g/(mg·min)) of the pseudo-second-order kinetic model.
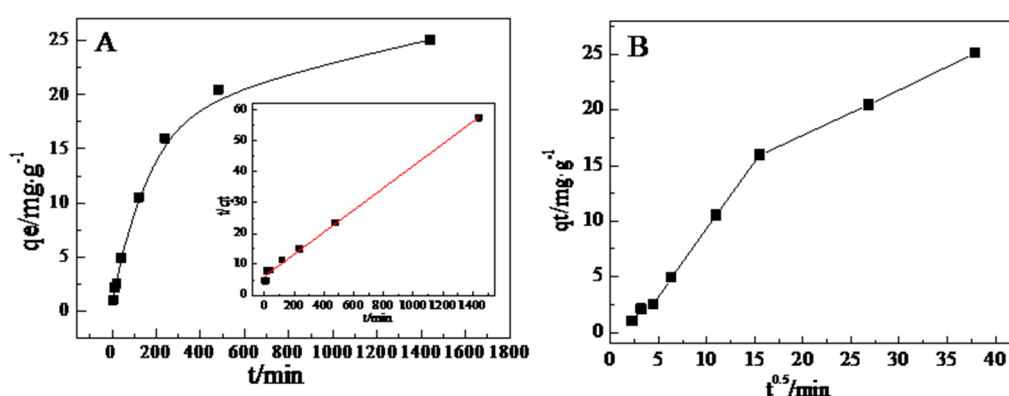

Figure 4. The adsorption kinetics of MPy-600 on Hg(II): (**A**) The pseudo-second-order model and (**B**) the Web-Morris model.

The fitting parameters of the pseudo-first-order and pseudo-second-order kinetic models are shown in Table 3. As presented in Figure 4, the results are fitted more accurately by the pseudo-second-order kinetic model (R^2 = 0.995) than the pseudo-first-order kinetic model (R^2 = 0.989) of Hg(II) on MPy-600, which follows that primary mechanism is chemical adsorption rather than physical adsorption.

Table 3. The fitted parameters of the pseudo-first-order model and pseudo-second-order kinetic model of Hg(II) sorption on MPy-600.

C_0 (mg/L)	Pseudo-First-Order			Pseudo-Second-Order		
	q_e (mg/g)	k_1	R^2	q_e (mg/g)	k_2	R^2
10	34.411	0.0038	0.952	27.925	0.0002	0.996

The Weber-Morris plot is used to describe the process of intraparticle diffusion. The Weber-Morris model can be expressed as

$$q_t = k \times t^{1/2} + c \tag{11}$$

where q_t (mg/g) represents the adsorbed amount at time t, k (mg/(g·min$^{1/2}$)) represents the rate constant, and c represents a constant. As shown in Figure 4B, the multilinear plots indicate that more than one mechanism might be responsible for Hg(II) adsorption onto MPy-600 [5].

The adsorption process can consist of two stages. The first stage from 0–20 min is for the surface adsorption or instantaneous adsorption on the most effective adsorbing sites of the MPy-600 surface. The second linear stage covering up to 20–40 min is for intraparticle diffusion. The primary effect is intraparticle diffusion, so the sorption rate slows down with increasing diffusion resistance until

the diffusion process reaches equilibrium. During the adsorption process, many other steps may be involved, but these steps may be indistinguishable from the two main stages [30,31]. The plot of q_t vs. $t^{1/2}$ of the second regression stage must be linear and pass through the origin, which proves that the mechanism of the intra-particle diffusion is controlled by the rate. In Figure 4B, the plot does not go across the origin, which may be ascribed to the distinction of the mass transfer rate of the starting and final adsorption stops. These results suggest that mainly controlling the mechanism for the sorption of Hg(II) onto MPy-600 is not intra-particle diffusion [27,32,33]. The relevant parameters are listed in Table 4.

Table 4. Kinetic Parameters of the Weber-Morris Model.

Sample	Parameters		R^2
MPy-600	$K_1 = 1.78$	$C_1 = -4.20$	0.9997
	$K_2 = 0.60$	$C_2 = 14.12$	0.9997

3.6. Thermodynamics

The thermodynamic parameters reveal the reaction mechanism of Hg(II) sorption onto MPy-600. The fitting for the thermodynamic model of Hg(II) onto MPy-600 is shown in Figure 5. The related parameters, including the standard free energy change (ΔG), standard enthalpy change (ΔH), and the standard entropy change (ΔS) for adsorption process can be calculated as follows (Equations (12)–(14)):

$$\Delta G = -RT ln K_c \tag{12}$$

$$ln K_c = \frac{\Delta S}{R} - \frac{\Delta H}{RT} \tag{13}$$

$$ln K_d = (C_0 - C_e)/C_e \times (V/m) \tag{14}$$

where R (8.314 J/(mol·K)) represents the ideal gas constant, and T (K) represents the temperature in Kelvin. The parameter K_d (L/g) is the distribution coefficient. The constant $ln K_c$ (L/g) is the adsorption equilibrium constant obtained by plotting $ln K_d$ vs. C_e and then extrapolating C_e to zero.
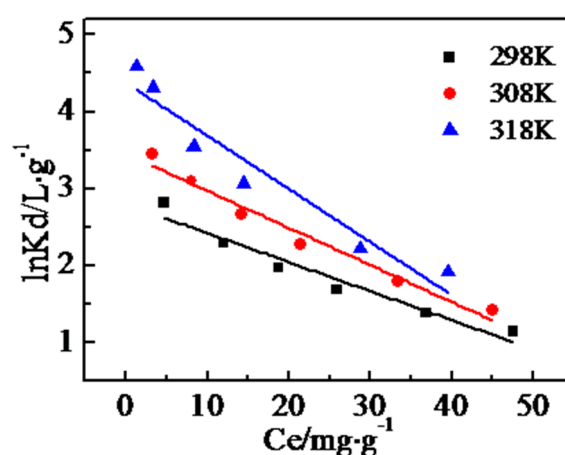

Figure 5. The linear plots of $ln K_d$ vs. C_e of Hg(II) onto MPy-600.

The line graphs of $ln K_d$ vs. C_e of Hg(II) adsorption onto MPy-600 at different temperatures are presented in Figure 5. The corresponding parameters for the sorption of Hg(II) onto MPy-600 are shown in Table 5. The negative ΔG values testify that the sorption of Hg(II) onto MPy-600 is a spontaneous process, and ΔG decreases as temperature is increasing, revealing that the sorption is more beneficial at higher temperatures. The positive ΔH value suggests this reaction process is endothermic. The positive ΔS implies that the molecular arrangement becomes more chaotic during

the reaction process, which leads to an increasing disorder in the reaction system, and the Hg(II) adsorption process is driven by enthalpy. The value of ΔS is between 0 and 22 J/(mol·K), which indicates that both physical and chemical adsorption processes exist during the adsorption.

Table 5. Thermodynamic parameters for the sorption of Hg(II) on MPy-600.

T (K)	ΔG (kJ/mol)	ΔH (kJ/mol)	ΔS (J/(mol·K))
298	−0.6930		
308	−0.8843	62.0557	0.2310
318	−1.1569		

3.7. Magnetization

As shown in Figure 6, the magnetic property of natural pyrite and MPy-600 are measured with the applied field of −45,000–45,000 Oe at room temperature. The pyrite shows a negligible magnetization, and the saturation magnetization of it is just 0.1 emu/g. However, the excellent magnetization of MPy-600 makes it possible to separate the sample from the solution by magnetic separation, which has a high saturation magnetization of 13.3 emu/g. The coercivity of MPy-600is 61.75, and Oe indicates an obvious magnetization hysteresis. MPy-600 does not show superparamagnetism, and the permanent magnetization is as low as 4.278 emu/g. The saturation magnetization of MPy-600 after adsorption decreases to 12 emu/g [20,34]. Thus, the magnetic property of MPy-600 guarantees the convenient magnetic separation from the aqueous solution in adsorption applications.
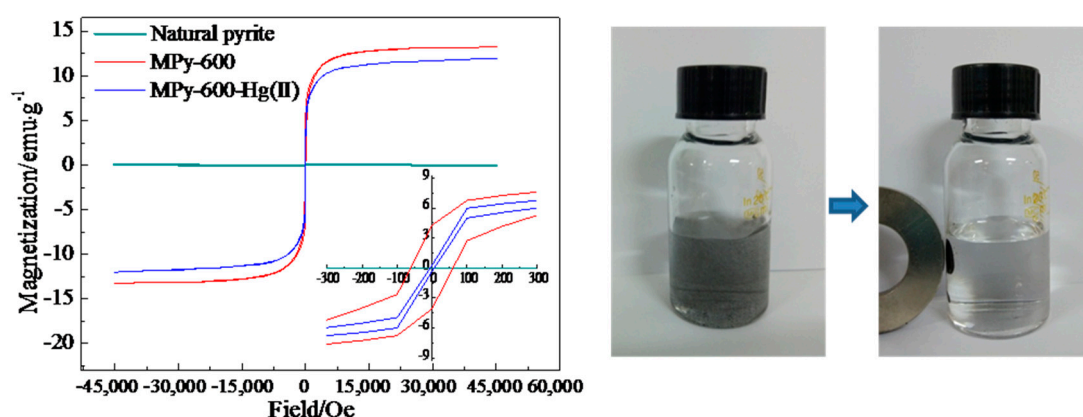

Figure 6. Magnetization characteristics of natural pyrite, MPy600, and MPy-600 after adsorption.

3.8. Adsorption Mechanism

3.8.1. XRD Analyses

Figure 7 shows the XRD pattern of MPy-600 after Hg(II) adsorption compared to the PDF standard card of pyrrhotite and HgS. From the figure, the reflections at 30.1°, 34.0°, 43.9°, and 53.2° correspond to the pyrrhotite [22]. Compared to the standard sample peaks of cinnabar, the peaks at 2θ = 26.5° of the reacted MPy-600 material are evident, which indicates that HgS is formed. The intensity of the peaks is relatively low for HgS compared to that of MPy-600, which reveals a lower content. Furthermore, the XRD pattern of the used MPy-600 preliminarily illustrates that the removal of Hg(II) onto MPy-600 is owing to the form of the HgS from the chemical reaction.
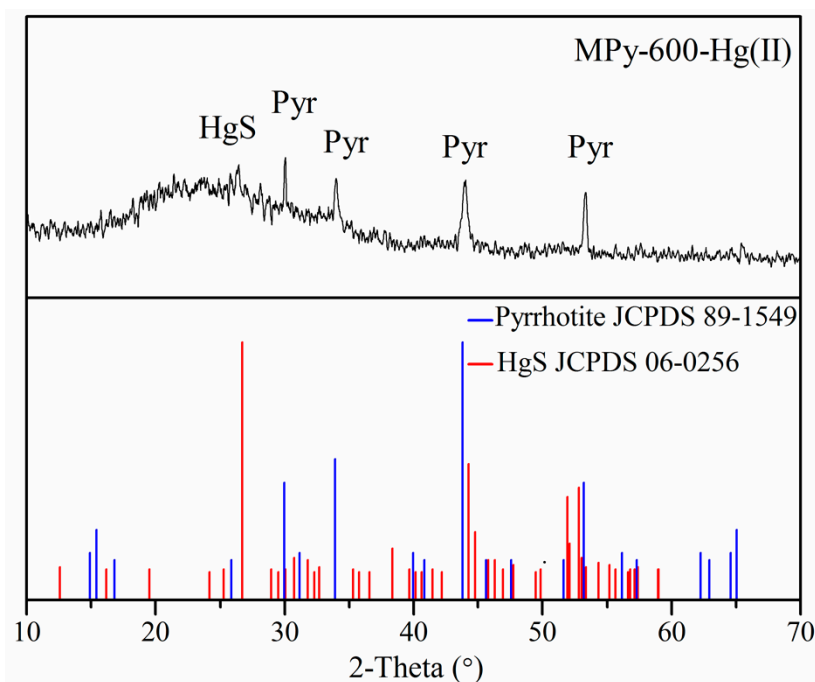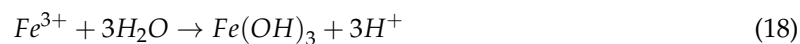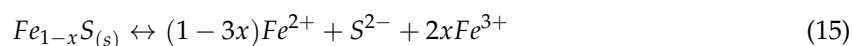
Figure 7. The XRD pattern of the reacted MPy-600 material. Pyr—pyrrhotite.

3.8.2. The FTIR and Raman Spectra

The FTIR spectra of MPy-600 and Hg(II)-adsorbed MPy-600 are exhibited in Figure 8A. The characteristic absorbance lines at 1076 cm^{-1} and 483 cm^{-1} are assigned to pyrrhotite. The peak at 3649 cm^{-1} refers to the −OH vibrations [12,35]. The characteristic absorbance peak at 3649 cm^{-1} of MPy-600-Hg(II) is higher, which can be ascribed to the formation of ferric hydroxide from the dissolution of iron, and more Hg(OH)$_2$ is formed by attracting more −OH molecules to Hg(II) [36]. The relative intensities of the MPy-600-Hg(II) peaks at 483 cm^{-1} and 1076 cm^{-1} are lower, which probably suggests that MPy-600 reacted with Hg(II) [37]. This result is consistent with XRD results, and the equations are as follows (Equations (15)–(20)):

$$Fe_{1-x}S_{(s)} \leftrightarrow (1-3x)Fe^{2+} + S^{2-} + 2xFe^{3+} \tag{15}$$

$$Hg^{2+} + S^{2-} \rightarrow HgS \tag{16}$$

$$Hg^{2+} + 2OH^- \rightarrow Hg(OH)_2 \tag{17}$$

$$Fe^{3+} + 3H_2O \rightarrow Fe(OH)_3 + 3H^+ \tag{18}$$

$$K_{sp} \; of \; FeS = \left[Fe^{2+} \right] \left[S^{2-} \right] = 1.59 \times 10^{-19} \tag{19}$$

$$K_{sp} \; of \; HgS = \left[Hg^{2+} \right] \left[S^{2-} \right] = 6.44 \times 10^{-53} \tag{20}$$
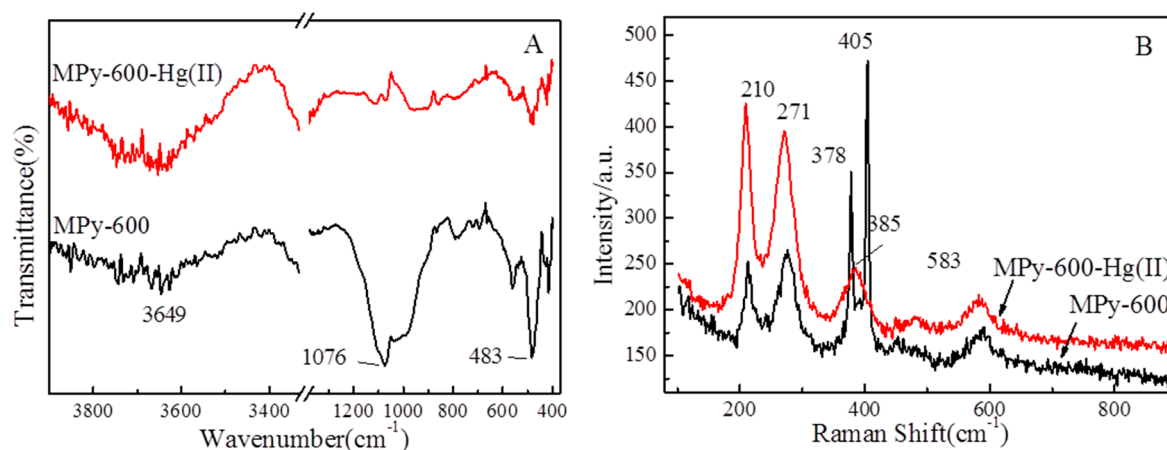
Figure 8. (**A**) The FTIR and (**B**) Raman spectra of MPy-600 and MPy-600 after Hg(II) adsorption.

The Raman spectra of MPy-600 and MPy-600 after Hg(II) sorption are presented in Figure 8B. Some research studies have shown that the frequency window of pyrrhotite vibrations is approximately 300–450 cm^{-1}. As exhibited in Figure 8B, the distinct vibration peaks at 378cm^{-1} and 405 cm^{-1} are consistent with vibrations of the Fe–S band to pyrrhotite [38,39]. The stretching vibrational frequency of Hg–S is approximately at 180–400 cm^{-1}. Therefore, the bands observed at 210 cm^{-1} and 271 cm^{-1} are ascribed to the S–Hg–S oscillations [35]. The weak and broad peak at 385 cm^{-1} is ascribed to a reduction in MPy-600, which is involved in the response [40]. The formation of a band at 583 cm^{-1} belongs to FeOOH (RRUFF). The appearance of the Hg-S band confirms the removal capacity of MPy-600 on Hg(II) [35].

3.8.3. XPS Analyses

The XPS is applied to characterize the elemental states to reveal the mechanism of Hg(II) adsorption onto MPy-600 [41]. The XPS spectrogram for Hg 4f, Fe 2p, S 2p, and O 1s of MPy-600 before and after the reaction is presented in Figure 9. As presented in Figure 9a,d, the Fe 2p peaks correspond to the fresh and used MPy-600, respectively. The fresh MPy-600 has four obvious peaks of Fe 2p on its surface. The binding energies centered at approximately 711.5 eV, 715.5 eV, and 723.8 eV may be assigned to Fe^{2+} bonded with S^{2-}, Fe^{3+} bonded with −OH, and Fe^{2+} bonded with SO$_4{}^{2-}$, respectively. Among them, the peaks at 711.5 eV and 724.9 eV assign to the Fe 2p3/2 and Fe 2p1/2 peaks (split both by 13.1eV), respectively. The used MPy-600 has four obvious Fe 2p peaks. These peaks are positioned at an offset to certain peak values. The binding energies centered at approximately 710.6 eV, 713.2 eV, and 719 eV may be ascribed to Fe^{2+} bonded with S^{2-}, Fe^{3+} bonded with –OH, and Fe^{2+} bonded with SO$_4{}^{2-}$, respectively. As shown in Figure 9a,d, the percentage increase in Fe^{2+} can be ascribed to Fe$_{1-x}$S dissolved to Fe^{2+} and S^{2-} and iron diffused to the surface from the interior [42]. The increasing Fe-oxide peaks reveal that MPy-600 is oxidized with increasing reaction time.
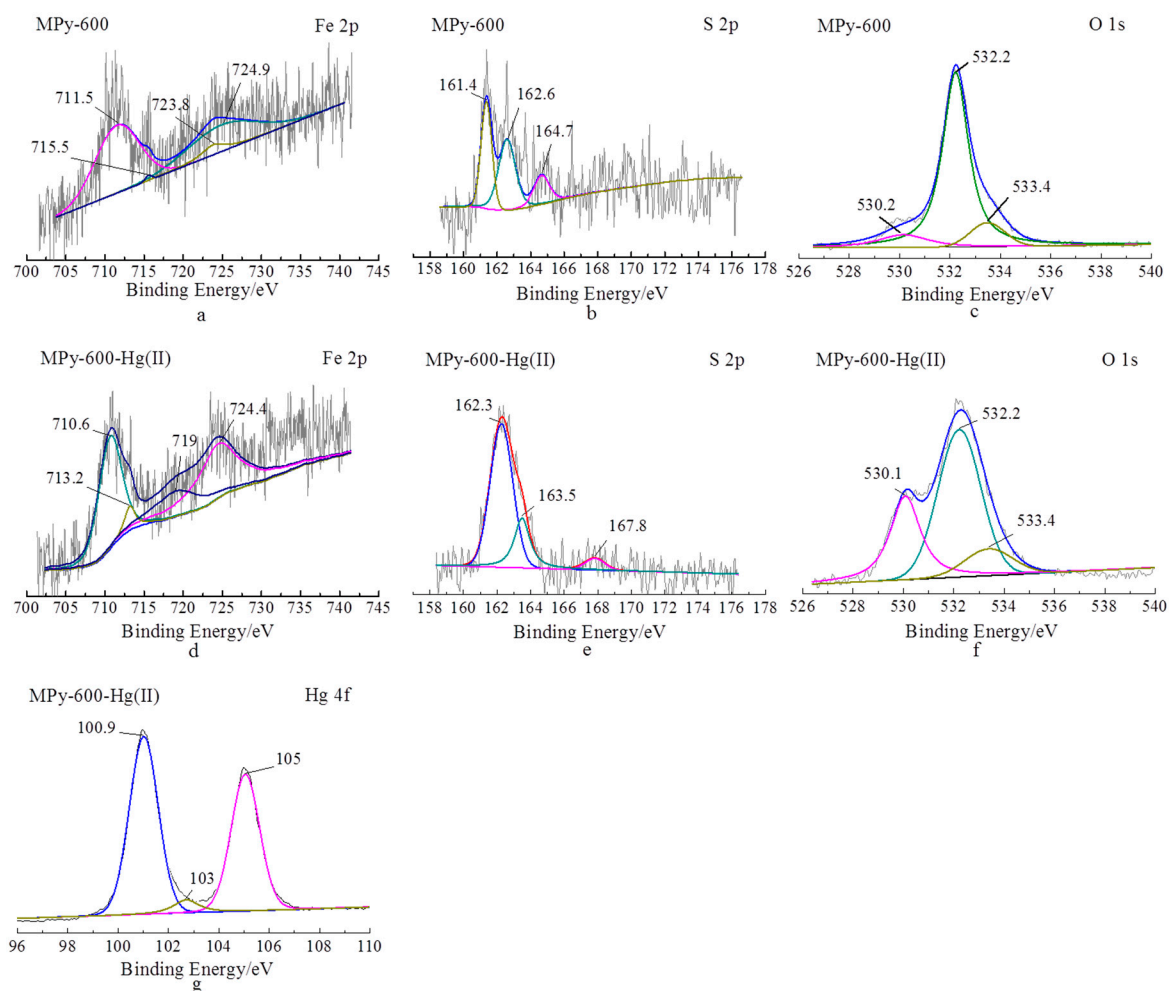
Figure 9. XPS spectra of MPy-600 (**a–c**) and MPy-600 after Hg(II) adsorption(**d–g**) in the Fe 2p, O 1s, S 2p, and Hg 4f spectral regions.

As observed in Figure 9b,e, the S 2p peak of MPy-600 centered at 161.4 eV is ascribed to S^{2-}, and the values at 162.6 eV and 164.7 eV represent S_2^{2-} and SO_4^{2-}, respectively [43]. In addition, the peak positions of MPy-600 after the removal of Hg(II) shifted to high energies because the surface electrons need plenty of energy for removal. The S 2p spectra of MPy-600 after Hg(II) adsorption exhibited peaks at 162.3 eV, 163.5 eV, and 167.8 eV that are ascribed to S^{2-}, S_2^{2-}, and SO_4^{2-}, respectively [34]. The amount of S^{2-} significantly increases after adsorption, which is ascribed to the dissolution of $Fe_{1-x}S$ and the formation of HgS. The amount of S_2^{2-} decreases because the S_2^{2-} is oxidized to disulfide and sulfate [44]. The oxidation of adsorbed Hg(II) mainly involved S_2^{2-} on MPy-600, from which it can be deduced that the percent of S_2^{2-} on MPy-600 has declined dramatically after Hg(II) adsorption [45].

As observed in Figure 9c,f, the O 1s at 530.2 eV ascribed to O^{2-} sufficiently exists on MPy-600. The binding energy appeared at 532.2 eV, which is owing to the O in the SO_4^{2-}. In addition, the binding energy of the O 1s spectrum at 533.4 eV is attributed to the O in the SiO_2. The higher spectral peaks are ascribed to iron diffusion, and when combined with minute amounts of oxygen, hydroxide, and water, ferric-hydroxides are formed [20]. Figure 9g exhibits the Hg 4f spectrum of MPy-600 after Hg(II) removal. The bond energies of Hg 4f7/2 at 100.9 eV and Hg 4f5/2 at 105 eV correspond to Hg^{2+} bonded with S^{2-}. Therefore, the above XPS conclusions confirmed that the HgS successfully formed on MPy-600. The other peak at 103 eV appeared, which could be due to the Si 2p of the SiO_2 [46]. Therefore, it suggested that the adsorption of Hg(II) by MPy-600 is mainly ascribed to the formation of HgS as the result of a chemical reaction.

3.8.4. SEM and TEM Analyses

The major composition and surface morphology of Hg(II) on the used MPy-600are characterized by SEM. Figure 10a shows the formation of a large number of new particles on the surface after Hg(II) adsorption, which has a nanometer-sized and plate-like shape. Compared to MPy-600 before adsorption, it can be derived that HgS is formed on the MPy-600. The content of Hg(II) in the EDS confirms the above discourse [16]. Figure 10b displays the SEM images with an EDX mapping of the MPy-600 after the reaction. In the Hg-EDX map, the distribution of the points which are characterized by the concentration of Hg(II) suggests the discrete Hg phase has formed. In the S-EDX map, the distribution of the points suggests the removal of Hg(II) is mainly ascribed to the form of HgS. SEM analysis of the used MPy-600 indicates that a large amount of HgS is produced of the material surface. Hence, it can be inferred that the reaction is driven by the solubility products of the sulfides and pyrrhotite, and the form of HgS is the principal factor of Hg(II) removal.
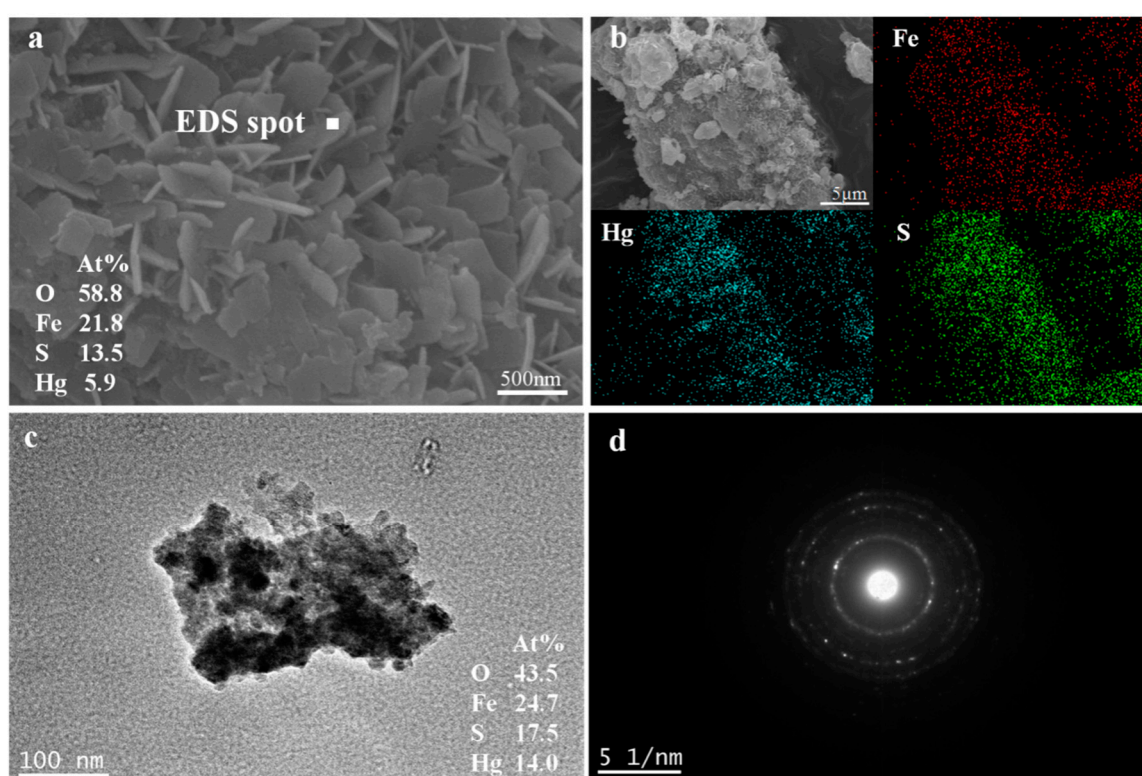

Figure 10. (**a**) SEM-EDS characterization. (**b**) SEM image with EDX mapping for different elements (Fe, S, and Hg). (**c**) TEM image, and (**d**) electron diffraction spot pattern of the used MPy-600.

As observed in Figure 10c, the diameter of the used MPy-600 particles is on a nanoscale. In addition, the EDS indicates that 14% Hg is detected. As shown in Figure 10d, the diffraction ring pattern of the specimen indicates that the material is polycrystalline [47]. The diffraction ring diameters are 3.3 Å, 2.45 Å, and 2.07 Å, which are indexed to the (101), (103), and (110) planes of cinnabar, respectively. In conclusion, HgS formed on theMPy-600 surface after the Hg(II) sorption. These results are in accordance with the proposed analysis. Therefore, it can be inferred that the primary mechanism on Hg(II) removal by MPy-600 is via a chemical reaction.

3.8.5. Product Analyses

The proportion of mercury precipitation in the products is evaluated by soaking the MPy-600 after reaction with 0.5% HCl to remove the $Hg(OH)_2$ and then measuring the content of residual Hg(II)in the leachate. According to the result, the content of $Hg(OH)_2$ accounts for 13% of the total Hg(II)

adsorption capacity. Therefore, it demonstrates that the Hg(II) sorption was mainly ascribed by the form of the HgS.

4. Conclusions

In this study, batch experiments were conducted to explore the property of MPy derived from the decomposition of pyrite with the adsorption of Hg(II). The experiments showed that the removal of Hg(II) onto MPy-600 can be effectively simulated by the Langmuir model with the maximum adsorptivity of 166.67 mg/g. The sorption of Hg(II) was raised as the pH increased from 2–6. The sorption of Hg(II) onto MPy-600 increased as the ionic strength increased, reflecting that the outer surface complexation was mainly a controlling factor in the reaction. The sorption of Hg(II) ontoMPy-600 can be fitted effectively by a pseudo-second-order kinetic model (R^2 = 0.995). The fitting of the thermodynamic model of Hg(II) on MPy-600 indicated that the reaction process is endothermic, spontaneous, and driven by entropy. Hg(II)-loaded MPy-600 can be easily removed from solution using magnetic separation through its magnetic property. From all the studies, the removal of Hg(II) by MPy-600 is ascribed to the chemical reactions and electrostatic attraction between negative charges in MPy-600 and the positive charges of Hg(II). This research proves that MPy is a highly effective sorbent for Hg(II) sorption. Therefore, the high property of MPy-600 for Hg(II) removal indicates that MPy can play a crucial role as a suitable substance for the removal for Hg(II) on iron sulfide in environmental purification territory.

Author Contributions: Conceptualization, P.L. (Ping Lu) and T.C.; methodology, H.L.; validation, P.L. (Ping Li), S.P. and Y.Y.; formal analysis, P.L. (Ping Lu); investigation, P.L. (Ping Lu); resources, T.C.; data curation, H.L.; writing—original draft preparation, P.L. (Ping Lu); writing—review and editing, P.L. (Ping Lu); visualization, P.L. (Ping Lu); supervision, T.C.; project administration, H.L.; funding acquisition, T.C.

Conflicts of Interest: The authors declare no conflict of interest.

References

1. Huang, J.; Wu, Z.; Chen, L.; Sun, Y. The sorption of Cd(II) and U(VI) on sepiolite: A combined experimental and modeling studies. *J. Mol. Liq.* **2015**, *209*, 706–712. [CrossRef]
2. Liu, T.; Xue, L.; Guo, X.; Liu, J.; Huang, Y.; Zheng, C. Mechanisms of Elemental Mercury Transformation on alpha-Fe$_2$O$_3$(001) Surface from Experimental and Theoretical Study: Influences of HCl, O$_2$, and SO$_2$. *Environ. Sci. Technol.* **2016**, *50*, 13585–13591. [CrossRef] [PubMed]
3. Huang, S.; Ma, C.; Liao, Y.; Min, C.; Du, P.; Jiang, Y. Removal of Mercury(II) from Aqueous Solutions by Adsorption on Poly(1-amino-5-chloroanthraquinone) Nanofibrils: Equilibrium, Kinetics, and Mechanism Studies. *J. Nanomater.* **2016**, *2016*, 1–11. [CrossRef]
4. Wajima, T.; Sugawara, K. Adsorption behaviors of mercury from aqueous solution using sulfur-impregnated adsorbent developed from coal. *Fuel Process. Technol.* **2011**, *92*, 1322–1327. [CrossRef]
5. Dash, S.; Chaudhuri, H.; Gupta, R.; Nair, U.G.; Sarkar, A. Fabrication and Application of Low-Cost Thiol Functionalized Coal Fly Ash for Selective Adsorption of Heavy Toxic Metal Ions from Water. *Ind. Eng. Chem. Res.* **2017**, *56*, 1461–1470. [CrossRef]
6. Wang, J.; Deng, B.; Chen, H.; Wang, X.; Zheng, J. Removal of Aqueous Hg(II) by Polyaniline: Sorption Characteristics and Mechanisms. *Environ. Sci. Technol.* **2009**, *43*, 5223–5228. [CrossRef]
7. Zhang, F.S.; Nriagu, J.O.; Itoh, H. Mercury removal from water using activated carbons derived from organic sewage sludge. *Water Res.* **2005**, *39*, 389. [CrossRef]
8. Cui, H.; Qian, Y.; Li, Q.; Wei, Z.; Zhai, J. Fast removal of Hg(II) ions from aqueous solution by amine-modified attapulgite. *Appl. Clay Sci.* **2013**, *72*, 84–90. [CrossRef]
9. Kadirvelu, K.; Kavipriya, M.; Karthika, C.; Vennilamani, N.; Pattabhi, S. Mercury (II) adsorption by activated carbon made from sago waste. *Carbon* **2004**, *42*, 745–752. [CrossRef]

10. Kadirvelu, K.; Kanmani, P.; Senthilkumar, P.; Subburam, V. Separation of Mercury(II) from Aqueous Solution by Adsorption onto an Activated Carbon Prepared from Eichhornia crassipes. *Adsorpt. Sci. Technol.* **2004**, *22*, 207–222. [CrossRef]

11. Tuzen, M.; Sari, A.; Mendil, D.; Soylak, M. Biosorptive removal of mercury(II) from aqueous solution using lichen (Xanthoparmelia conspersa) biomass: Kinetic and equilibrium studies. *J. Hazard. Mater.* **2009**, *169*, 263–270. [CrossRef] [PubMed]

12. Wang, X.; Lv, P.; Zou, H.; Li, Y.; Li, X.; Liao, Y. Synthesis of Poly(2-aminothiazole) for Selective Removal of Hg(II) in Aqueous Solutions. *Ind. Eng. Chem. Res.* **2016**, *55*, 4911–4918. [CrossRef]

13. Couture, R.M.; Rose, J.; Kumar, N.; Mitchell, K.; Wallschlager, D.; van Cappellen, P. Sorption of arsenite, arsenate, and thioarsenates to iron oxides and iron sulfides: A kinetic and spectroscopic investigation. *Environ. Sci. Technol.* **2013**, *47*, 5652–5659. [CrossRef] [PubMed]

14. Ma, B.; Kang, M.; Zheng, Z.; Chen, F.; Xie, J.; Charlet, L.; Liu, C. The reductive immobilization of aqueous Se(IV) by natural pyrrhotite. *J. Hazard. Mater.* **2014**, *276*, 422–432. [CrossRef] [PubMed]

15. Chen, T.; Yang, Y.; Li, P.; Liu, H.; Xie, J.; Xie, Q.; Zhan, X. Performance and characterization of calcined colloidal pyrite used for copper removal from aqueous solutions in a fixed bed column. *Int. J. Miner. Process.* **2014**, *130*, 82–87. [CrossRef]

16. Yang, Y.; Chen, T.; Li, P.; Liu, H.; Xie, J.; Xie, Q.; Zhan, X. Removal and Recovery of Cu and Pb from Single-Metal and Cu–Pb–Cd–Zn Multimetal Solutions by Modified Pyrite: Fixed-Bed Columns. *Ind. Eng. Chem. Res.* **2014**, *53*, 18180–18188. [CrossRef]

17. Chen, T.; Shi, Y.; Liu, H.; Chen, D.; Li, P.; Yang, Y.; Zhu, X. A novel way to prepare pyrrhotite and its performance on removal of phosphate from aqueous solution. *Desalin. Water Treat.* **2016**, *57*, 23864–23872. [CrossRef]

18. Chen, T.H.; Wang, J.Z.; Wang, J.; Xie, J.J.; Zhu, C.Z.; Zhan, X.M. Phosphorus removal from aqueous solutions containing low concentration of phosphate using pyrite calcinate sorbent. *Int. J. Environ. Sci. Technol.* **2014**, *12*, 885–892. [CrossRef]

19. Liu, H.; Zhu, Y.; Xu, B.; Li, P.; Sun, Y.; Chen, T. Mechanical investigation of U(VI) on pyrrhotite by batch, EXAFS and modeling techniques. *J. Hazard. Mater.* **2017**, *322*, 488–498. [CrossRef]

20. Liao, Y.; Chen, D.; Zou, S.; Xiong, S.; Xiao, X.; Dang, H.; Chen, T.; Yang, S. Recyclable Naturally Derived Magnetic Pyrrhotite for Elemental Mercury Recovery from Flue Gas. *Environ. Sci. Technol.* **2016**, *50*, 10562–10569. [CrossRef]

21. Li, R.; Kelly, C.; Keegan, R.; Xiao, L.; Morrison, L.; Zhan, X. Phosphorus removal from wastewater using natural pyrrhotite. *Colloids Surf. A Physicochem. Eng. Asp.* **2013**, *427*, 13–18. [CrossRef]

22. Janzen, M.P.; Nicholson, R.V.; Scharer, J.M. Pyrrhotite reaction kinetics: Reaction rates for oxidation by oxygen, ferric iron, and for nonoxidative dissolution. *Geochim. Et Cosmochim. Acta* **2000**, *64*, 1511–1522. [CrossRef]

23. Hu, G.; Dam-Johansen, K.; Wedel, S.; Hansen, J.P. Decomposition and oxidation of pyrite. *Prog. Energy Combust. Sci.* **2006**, *32*, 295–314. [CrossRef]

24. Sanhueza, V.; Kelm, U.; Cid, R. Synthesis of molecular sieves from Chilean kaolinites: 1. Synthesis of NaA type zeolites. *J. Chem. Technol. Biotechnol.* **1999**, *74*, 358–363. [CrossRef]

25. Widler, A.M.; Seward, T.M. The adsorption of gold(I) hydrosulphide complexes by iron sulphide surfaces. *Geochim. Et Cosmochim. Acta* **2002**, *66*, 383–402. [CrossRef]

26. Duan, S.; Liu, X.; Wang, Y.; Shao, D.; Alharbi, N.S.; Alsaedi, A.; Li, J. Highly efficient entrapment of U(VI) by using porous magnetic $Ni_{0.6}Fe_{2.4}O_4$ micro-particles as the adsorbent. *J. Taiwan Inst. Chem. Eng.* **2016**, *65*, 367–377. [CrossRef]

27. Liu, P.; Yuan, N.; Xiong, W.; Wu, H.; Pan, D.; Wu, W. Removal of Nickel(II) from Aqueous Solutions Using Synthesized β-Zeolite and Its Ethylenediamine Derivative. *Ind. Eng. Chem. Res.* **2017**, *56*, 3067–3076. [CrossRef]

28. Sun, Y.; Lou, Z.; Yu, J.; Zhou, X.; Lv, D.; Zhou, J. Immobilization of mercury (II) from aqueous solution using Al_2O_3-supported nanoscale FeS. *Chem. Eng. J.* **2017**, *323*, 483–491. [CrossRef]

29. Jin, Z.; Wang, X.; Sun, Y.; Ai, Y.; Wang, X. Adsorption of 4-n-Nonylphenol and Bisphenol-A on Magnetic Reduced Graphene Oxides: A Combined Experimental and Theoretical Studies. *Environ. Sci. Technol.* **2015**, *49*, 9168–9175. [CrossRef]

30. Weng, C.H.; Pan, Y.-F. Adsorption characteristics of methylene blue from aqueous solution by sludge ash. *Colloids Surf. A Physicochem. Eng. Asp.* **2006**, *274*, 154–162. [CrossRef]

31. Liu, N.; Charrua, A.B.; Weng, C.H.; Yuan, X.L.; Ding, F. Characterization of biochars derived from agriculture wastes and their adsorptive removal of atrazine from aqueous solution: A comparative study. *Bioresour. Technol.* **2015**, *198*, 55. [CrossRef] [PubMed]

32. Xu, Y.; Zeng, X.; Zhang, B.; Zhu, X.; Zhou, M.; Zou, R.; Sun, P.; Luo, G.; Yao, H. Experiment and Kinetic Study of Elemental Mercury Adsorption over a Novel Chlorinated Sorbent Derived from Coal and Waste Polyvinyl Chloride. *Energy Fuels* **2016**, *30*, 10635–10642. [CrossRef]

33. Deze, E.G.; Papageorgiou, S.K.; Favvas, E.P.; Katsaros, F.K. Porous alginate aerogel beads for effective and rapid heavy metal sorption from aqueous solutions: Effect of porosity in Cu^{2+} and Cd^{2+} ion sorption. *Chem. Eng. J.* **2012**, *209*, 537–546. [CrossRef]

34. Yang, S.; Yan, N.; Guo, Y.; Wu, D.; He, H.; Qu, Z.; Li, J.; Zhou, Q.; Jia, J. Gaseous elemental mercury capture from flue gas using magnetic nanosized $(Fe_{3-x}Mn_x)1$-deltaO_4. *Environ. Sci. Technol.* **2011**, *45*, 1540–1546. [CrossRef] [PubMed]

35. Andac, M.; Mirel, S.; Senel, S.; Say, R.; Ersoz, A.; Denizli, A. Ion-imprinted beads for molecular recognition based mercury removal from human serum. *Int. J. Biol. Macromol.* **2007**, *40*, 159–166. [CrossRef] [PubMed]

36. Zhu, Y.; Chen, T.; Liu, H.; Xu, B.; Xie, J. Kinetics and thermodynamics of Eu(III) and U(VI) adsorption onto palygorskite. *J. Mol. Liq.* **2016**, *219*, 272–278. [CrossRef]

37. Gong, Y.; Liu, Y.; Xiong, Z.; Zhao, D. Immobilization of mercury by carboxymethyl cellulose stabilized iron sulfide nanoparticles: Reaction mechanisms and effects of stabilizer and water chemistry. *Environ. Sci. Technol.* **2014**, *48*, 3986–3994. [CrossRef] [PubMed]

38. Wang, A.; Jolliff, B.L.; Haskin, L.A. Raman spectroscopic characterization of a Martian SNC meteorite: Zagami. *J. Geophys. Res. Planets* **1999**, *104*, 8509–8519. [CrossRef]

39. Frost, R.L.; Martens, W.N.; Kloprogge, J.T. Raman spectroscopic study of cinnabar (HgS), realgar (As_4S_4), and orpiment (As_2S_3) at 298 and 77K. *Neues Jahrb. Für Miner. Mon.* **2002**, *2002*, 469–480. [CrossRef]

40. Szuskiewicz, B.W.W. Raman spectroscopy of cubic HgS Fe. *Acta Phys. Pol. A* **1995**, *87*, 416–418.

41. Sun, Y.; Yang, S.; Chen, Y.; Ding, C.; Cheng, W.; Wang, X. Tuning the chemistry of graphene oxides by a sonochemical approach: Application of adsorption properties. *Environ. Sci. Technol.* **2015**, *49*, 4255–4262. [CrossRef] [PubMed]

42. Bone, S.E.; Bargar, J.R.; Sposito, G. Mackinawite (FeS) reduces mercury(II) under sulfidic conditions. *Environ. Sci. Technol.* **2014**, *48*, 10681–10689. [CrossRef] [PubMed]

43. Pratt, A.R.; Muir, I.J.; Nesbitt, H.W. X-ray photoelectron and Auger electron spectroscopic studies of pyrrhotite and mechanism of air oxidation. *Geochim. Et Cosmochim. Acta* **1994**, *58*, 827–841. [CrossRef]

44. Knipe, S.W.; Mycroft, J.R.; Pratt, A.R.; Nesbitt, H.W.; Bancroff, G.M. X-ray photoelectron spectroscopic study of water adsorption on iron sulphide minerals. *Geochim. Et Cosmochim. Acta* **1995**, *59*, 1079–1090. [CrossRef]

45. Philippe, B.; Pascale, B.G.; Marc, A.; Renaud, R.; Jean, J.E. XPS and XAS Study of the Sorption of Hg(II) onto Pyrite. *Langmuir* **2001**, *17*, 3970–3979.

46. Bootharaju, M.S.; Pradeep, T. Uptake of Toxic Metal Ions from Water by Naked and Monolayer Protected Silver Nanoparticles: An X-ray Photoelectron Spectroscopic Investigation. *J. Phys. Chem. C* **2010**, *114*, 8328–8336. [CrossRef]

47. Temgire, M.K.; Joshi, S.S. Optical and structural studies of silver nanoparticles. *Radiat. Phys. Chem.* **2004**, *71*, 1039–1044. [CrossRef]